Journal of Inorganic and Organometallic Polymers and Materials
https://doi.org/10.1007/s10904-023-02974-5

RESEARCH

The Role of Cobalt Ferrites Nanoparticles on Structural and Electrochemical Properties of Mesoporous Silica for Supercapacitor Applications

Reda. S. Salama[1] · Riyadh H. Alshammari[2] · Ayman Nafady[2] · Razium Ali Soomro[3] · Mostafa S. Gouda[1] · Fathi S. Awad[4,5]

Received: 27 August 2023 / Accepted: 18 December 2023

Abstract
The research focuses on enhancing the energy storage capabilities of mesoporous silica (MCM-41) for supercapacitor applications. Electrodes made solely from MCM-41 do not possess the desired energy density required for electronic devices. To address this, combining ferrites with MCM-41 has been proposed as a means to enhance the electrochemical behavior. In this study, various contents of COF were loaded on MCM-41. Different characterization methods were used to study the physical and surface properties of the as synthesized materials like XRD, FTIR, SEM, TEM, EDX and SEM-mapping. TEM images confirmed that all the as-synthesized composites retained the mesoporous structure, and the particle size of ferrites ranged from 8 to 14 nm. The cyclic voltammetry (CV) and galvanostatic charge–discharge (GCD) techniques were employed to investigate the electrochemical characteristics of the composite materials in H_2SO_4 electrolyte solution (1.0 M) and a potential window ranging from 0.0 to 0.8 V. The results demonstrated that the incorporation of ferrites onto MCM-41 led to an elevation in specific capacitance, with the highest value (746 $F.g^{-1}$) observed at 35 COF-MCM-41 composite. However, further increasing the content of ferrites resulted in a decrease in specific capacitance. Furthermore, the prepared composites exhibited excellent cycling stability even after 5000 cycles, with MCM-41, COF, and 35 COF-MCM-41 retaining 84.4%, 89.4%, and 94.8% of their initial specific capacitance, respectively. These findings highlight the significant role played by the dispersion of cobalt ferrite nanoparticles in enhancing pseudocapacitance behavior, thus improving the overall electrochemical performance of the composites.

Keywords Cobalt ferrites nanoparticles · Mesoporous silica · MCM-41 · Energy storage · Supercapacitors

1 Introduction

In recent years, the remarkable growth in various energy storage technologies, including electrochemical capacitors or supercapacitors, driven by sources like biomass, wind, and solar energy, has addressed the constraints of traditional batteries and fuel cells, offering superior power density, stability, and extended cycle life in electrical and electronic circuits[1]. Supercapacitors can be categorized into two primary mechanisms. The first mechanism involves electrical double layer capacitors (EDLCs), which offer numerous benefits like high porosity, extensive surface area, excellent electrical conductivity, and affordability. Nonetheless, they are accompanied by drawbacks like low energy density and specific capacitance. EDLCs primarily rely on non-faradaic reactions occurring between two electrodes and are typically fabricated using carbon-based materials like graphene

✉ Reda. S. Salama
dr.reda.salama@gmail.com; reda.salama@deltauniv.edu.eg

1 Basic Science Department, Faculty of Engineering, Delta University for Science and Technology, Gamasa, Egypt

2 Department of Chemistry, College of Science, King Saud University, 11451 Riyadh, Saudi Arabia

3 State Key Laboratory of Chemical Resource Engineering School of Chemistry, Beijing Advanced Innovation Center for Soft Matter Science and Engineering, Beijing 100029, People's Republic of China

4 Chemistry Department, Faculty of Science, Mansoura University, Mansoura 35516, Egypt

5 Department of Chemistry, Faculty of Science, New Mansoura University, New Mansoura City, Egypt

Published online: 23 January 2024

[2], activated carbon (AC) [3], carbon nanotubes [4], etc. Otherwise, pseudocapacitors exhibit remarkable energy density and specific capacitance due to redox reactions taking place at the surface of electrode materials. These materials can be metal oxides such as FeO [5], NiO [6], Al_2O_3 [7], SiO_2 [8],etc. or including conducting polymers (CPs) like polyaniline (PANI) [9], polypyrrole (PPy) [10], etc., but, these materials suffer from stability issues and tend to degrade after a limited cycles of charging and discharging process. Considering these two aspects of supercapacitor mechanisms, it is evident that the preparation of composite materials is necessary to overcome these limitations and improve the electrochemical activities of supercapacitor electrodes [11].

To align with the goal seven of sustainable development, particularly by utilizing cost-effective materials and environmentally friendly energy storage devices [12]. The utilization mesoporous silica (MCM-41) has emerged as a crucial precursor for silicon-based substances. MCM-41 be made up of a well-organized arrangement of cylindrical mesoporous structures with a hierarchical architecture, facilitating the efficient diffusion of electrolyte ions to electrode materials. Additionally, MCM-41 possesses various other beneficial characteristics such as hydrophilicity and the ability to support the reducibility of metal materials [13, 14]. Consequently, the incorporation of metal oxides materials into MCM-41 has shown promise in enhancing electrochemical performance, as indicated by previous research [15].

In recent times, Mesoporous silica is often employed as a supporting material in the synthesis of various nanocomposites due to its unique properties. When combined with cobalt ferrite in the context of supercapacitors, the choice is likely driven by several factors including high surface area, that providing more active sites for electrochemical reactions. This is crucial for enhancing the performance of supercapacitors as it allows for more charge storage. As well as, the porous structure of mesoporous silica facilitates faster ion diffusion within the material. This property is advantageous for supercapacitors, where rapid charge and discharge rates are desirable [16]. On the other hand, cobalt ferrite itself may not be highly conductive, but by incorporating mesoporous silica, which can act as a conductive scaffold, the overall electrical conductivity of the composite may be improved. This is important for efficient electron transport during the charge and discharge cycles of supercapacitors. Mesoporous silica can also help prevent the aggregation or agglomeration of cobalt ferrite nanoparticles, ensuring a more homogeneous distribution [17, 18]. This is essential for maintaining the integrity of the composite material and optimizing its electrochemical performance. Many researchers have verified that the introduction of ferrite or oxide surface matrices can lead to a significant enhancement in electrochemical storage performance, creating more active sites and extrinsic defects. Researchers have shown interest in spinal ferrites (MFe_2O_4), where "M" represents divalent metal ions like Zn, Mn, Co, Cu, Ni, Mg, and others, because of their affordability, excellent catalytic activity, abundance, electroconductivity, and high stability[19–22]. Moreover, the magneto strictive features of ferrites enable their rapid and easy separation in the reaction medium [23]. These characteristics collectively make ferrites well-suited for oxidation–reduction reactions, resulting in increased pseudocapacitance and enhanced electrochemical performance of supercapacitor electrodes [24].

Minakshi et al. reported on the utilization of various binary metal oxides, including $MgMoO_4$ [25], CaMoO4 [26], and $NiMoO_4$ [27], as exceptional electrode materials for pseudocapacitors. These metal oxides have demonstrated notable performance in supercapacitor applications, showcasing their potential as effective contributors to the development of high-performance energy storage systems.

In this research, varying weight ratios of nanoscale cobalt ferrite ($CoFe_2O_4$) were effectively deposited onto MCM-41, which was prepared using cetyltrimethylammonium bromide (CTAB) as a template and tetraethyl orthosilicate (TEOS) as a silicon precursor. The characteristics, surface modifications, and synthesis of the prepared nanocomposites were analyzed using different methods like XRD, FTIR, SEM, TEM, EDX and SEM-mapping. Additionally, the electrochemical activities of the nanocomposites was investigated using different measurements like CV, GCD, and EIS.

2 Materials and Methods

2.1 Materials

The chemical materials and reagents utilized in this study were sourced from multiple suppliers. Cobalt nitrate hexahydrate ($Co(NO_3)_2$. 6 $H_2O, > 99\%$) and hydrated iron nitrate $Fe(NO_3)_3{\cdot}9H_2O, > 99$) were purchased from Merck. CTAB and TEOS were obtained from Sigma-Aldrich. While, ammonia solution (33%), NaOH, KOH, HCl and N-methyl-2-pyrrolidone (NMP, 98%) and polyvinylidene fluoride (PVDF) was obtained from Loba Chemie. Besides, ethanol (99.8%) and graphite sheet were purchased from Fisher Chemical Companies and from XRD Carbon, China, respectively.

2.2 Composites Preparation

2.2.1 Preparation Mesoporous Silica (MCM-41)

MCM-41 was successfully synthesized following the previously reported procedure with some modifications [28, 29]. Typically, a clear aqueous solution of 100 ml containing 2.0

g CTAB was vigorously stirred and mixed with 12.5 ml of 33 wt% ammonia solution for 30 min. This led to the formation of an adequately alkaline solution with a pH spanning from 13.0 to 14.0. After the stirring, 10.0 ml of TEOS were gradually introduced into the solution's center. Manual stirring was employed to guarantee the thorough blending of the dense white mixture. The resultant white substance was later filtered, rinsed with deionized water, and then dried for a duration of one night at 120 °C within an electric oven.

2.2.2 Preparation of Pure and Supported Cobalt Ferrites

To prepare cobalt ferrites nanoparticles, a solution comprising 25 ml and containing 4.04 g of iron nitrate nonahydrate was combined with a solution of 25 ml containing 1.455 g of cobalt nitrate hexahydrate. The mixture was vigorously stirred for a duration of 2 h at a temperature of 60 °C. After two hours, a solution of 25 ml of 3.0 M NaOH was synthesized and slowly poured on the previous solution dropwise until the pH of the solution was reached to 11–12. Following the precipitation at the intended pH, the mixture was subjected to filtration and underwent three rounds of washing using distilled water. Subsequently, the filtrate was dried overnight at 80 °C and subsequently calcined in an open-air atmosphere at 550 °C for a duration of 3 h. As well as, cobalt ferrites@MCM-41 composites were prepared by the same methods with some modification. A mixture comprising a specific quantity of cobalt and iron nitrate was introduced to 2.0 g of calcined MCM-41 that was dispersed in 50 ml of distilled water. This process resulted in the creation of $CoFe_2O_4$ supported on MCM-41, with concentrations of 15.0, 35.0, and 55.0 wt.% respectively. The resulting pure and modified ferrites were labeled as COF, 15COF-MCM-41, 35COF-MCM-41, and 55COF-MCM-41 for cobalt ferrite, 15.0, 35 and 55.0 wt% $CoFe_2O_4$@MCM-41, respectively.

2.3 The Electrode Fabrication

To create a working electrode, a mixture was formed by combining 10.0% PVDF as a binder, 10.0% acetylene black and 80.0% of the prepared nanocomposites as the active material, with NMP to create a slurry. The graphite sheets, serving as the current collector, were treated to remove any remaining residues by rinsing them with 0.1 M HCl and then cleansing them with ethanol. The working electrode was created by delicately applying the nanocomposite mixture onto graphite sheets using small droplets, followed by thorough drying at a temperature of 60°C. The mass loading of active material on MCM-41, COF, 15COF-MCM-41, 35COF-MCM-41, and 55COF-MCM-41 as a working electrode were found to be 914, 1014, 937, 979, and 1014, respectively.

2.4 Characterization Techniques

The prepared nanocomposites were subjected to various characterization techniques. X-ray diffraction patterns (XRD) were acquired using the XRD-7000 Shimadzu-Japan instrument, operating at 40 kV and 30 mA with Cu-K radiation ($\lambda = 1.5$ Å). This facilitated the assessment of crystallinity and crystallite size using the Scherrer equation ($D = (0.89\lambda)/(\beta\cos\theta)$) [30–32]. Furthermore, Fourier Transform Infrared (FTIR) spectrophotometer (PerkinElmer-Spectrum 2B, USA), were applied from 400 to 4000 cm^{-1}. Additionally, the surface morphology and topography were analyzed using JEOL JSM-IT200 equipment (SEM), while transmission electron microscopy (TEM) was performed using the TEM-JEOL JEM-2100 LaB6 instrument. The chemical composition was determined through energy dispersive X-ray spectroscopy (EDX). Finally, pore size distributions and specific surface areas were determined using a BELSORP-mini II instrument at − 196 °C.

2.5 Electrochemical Measurements

In this study, Metrohm Auto lab Instruments Potentiostat and Galvanostat were used to assess electrochemical performance by configuring three-electrode systems. The setup consisted of a working electrode, a reference electrode (Ag/AgCl), and a counter electrode (platinum foil electrode). The test was examined in a 1.0 M H_2SO_4 aqueous electrolyte. To assess the electrochemical performance, specific capacitance (Cs) in F. g^{-1} was determined from cyclic voltammetry curves (CV) using Eq. (1). Galvanostatic charge–discharge (GCD) curves were also employed, and specific capacitance was calculated using Eq. (2). [3].

$$C_s(F/g) = \frac{\int_{Vi}^{Vf} I(V)dv}{2S \times m.\Delta V}, \tag{1}$$

$$C_s(F/g) = \frac{I \times t}{m \times \Delta V}, \tag{2}$$

where m is represents the mass of the active material loaded onto the working electrode in grams, S is the scan rate, measured in millivolts per second, ΔV is represents the potential window range, measured in volts, t represents the duration of the discharge current in seconds, and I is the magnitude of the discharge current, measured in amperes.

The preparation of the dual-electrode system can be configured as previously mentioned by Toyoko Imae et al. [33]. The working-electrode sensing (WE sense) and working-electrode power (WE power) connections from the electrochemical workstation were attached to one side of the cell. On the other side, the counter electrode (CE) and reference

electrode (RE) connections from the electrochemical workstation were combined. The two-electrode setup included two composite electrodes, either identical or dissimilar, fully enclosed within filter paper soaked in an electrolyte. The filter paper had dual roles: it absorbed and stored the electrolyte for the electrochemical reaction of the two-electrode system, while also functioning as a separator between the two composite electrodes. Once the electrodes were assembled, CV and GCD analysis was performed to calculate specific capacitance, power density, and energy density from Eqs. (3) and (4) as the following [34, 35]:

$$E(Wh/Kg) = \frac{Cs.V^2}{2} \times \frac{1000}{3600} \quad (3)$$

$$P(W/Kg) = \frac{E}{t} \times 3600 \quad (4)$$

3 Results and Discussion

3.1 XRD Measurements

XRD patterns of mesoporous silica, and x COF-MCM-41 composites were displayed in Fig. 1 and the figure showed that MCM-41 has a very broad band that is characteristics to amorphous silica as approved in the previously literature [36, 37]. Though, the amorphous peak of mesoporous silica became weaker, and the peaks related to cobalt ferrites appeared when the $COFe_2O_4$ NPs are presented into MCM-41 [38]. The peaks with 2θ values of 30.1, 35.7, 42.9, 56.9 and 63.1 correspond to the (220), (311), (400), (511) and (440) planes, respectively [39]. Crystallite size of $CoFe_2O_4$ NPs was calculated using Scherrer equation and was found to be 12.47, 7.87, 8.74, and 9.57 nm for COF, 15COF-MCM-41, 35COF-MCM-41, and 55COF-MCM-41, respectively. The results display that the ferrites nanoparticle sizes over MCM-41 are less than 10 nm compared with pure ferrites, which could be related to the good dispersion of ferrites on the MCM-41 surface that leads to decrease in the crystallite size.

3.1.1 FTIR Spectroscopy

FT-IR spectra were applied to identify the chemical bonding and functional groups of the prepared samples and presented in Fig. 2. Figure 2a displays the FTIR spectrum of MCM-41 which displayed that there were some bands that characteristics to mesoporous silica. Firstly, the band at wavenumber 1091 cm^{-1} is attributed to the asymmetric stretching vibration of the Si–O-Si group [40]. Additionally, the bands observed in the regions ranged from 800 to 970 cm^{-1} were attributed to the symmetrical vibration of Si–O-Si groups [41]. While, the bending vibration peaks of Si–O-Si was observed at wavelength of 462 cm^{-1} [42]. As well as, there was a broad band at wavenumber of 3445 cm^{-1} that related to the stretching vibration of silanol group peak at MCM-41 or the hydroxyl group of adsorbed water molecules [29]. While, the bending vibration of this silanol group was observed at wavenumber of 1639 cm^{-1} [43]. Otherwise, FTIR spectra of COF and X COF-MCM-41 were displayed in Fig. 2b–e. The spectra revealed that there are two main obvious bands were appeared at 583 and 462 cm^{-1}, which considered as a finger print for the ferrites NPs. These wavenumbers were related to higher (ν1) and lower frequency band (ν2) for cobalt ferrites that attributed to the tetrahedral and octahedral sites, respectively [44]. The main difference between them is the difference in the intensities of the main

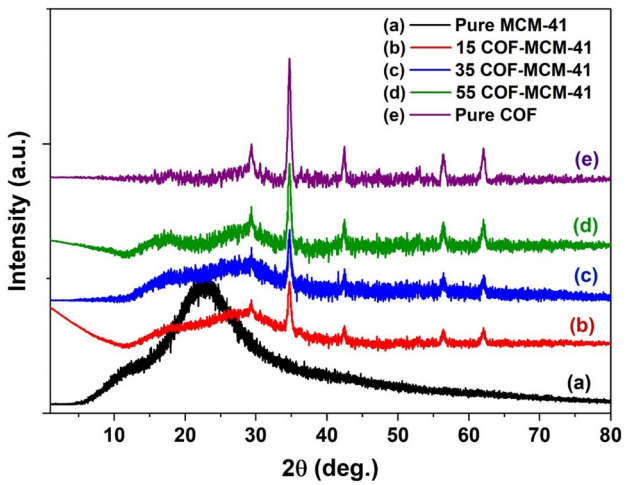

Fig. 1 XRD patterns of MCM-41, COF, 15COF-MCM-41, 35COF-MCM-41, and 55COF-MCM-41

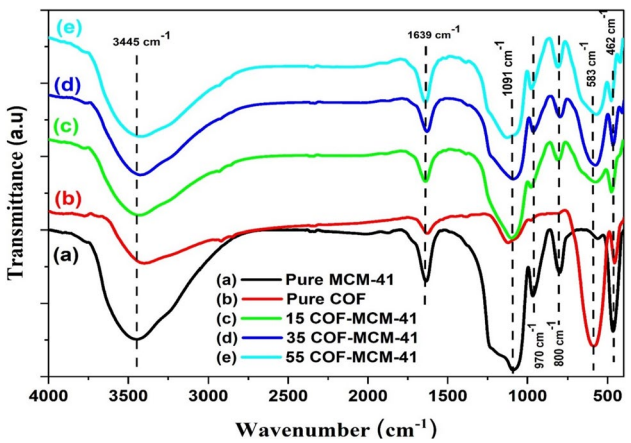

Fig. 2 FTIR spectra of **a** MCM-41, **b** COF, **c** 15COF-MCM-41, **d** 35COF-MCM-41, and **e** 55COF-MCM-41

two peaks of ferrites. The intensity of these two bands were increased with increasing the ferrites content until reached to the highest value at 55COF-MCM-41.

3.1.2 SEM, EDS and Elemental Mapping Analysis

Figure 3a–e demonstrated the SEM images of all the prepared samples. The figure displayed that mesoporous MCM-41 has spherical particles formation, and this spherical structure was preserved even after modification with different contents of $CoFe_2O_4$. As well as, the figure revealed that there is no clear ferrites accumulation were displayed and this indicates that ferrites nanoparticles were well dispersed on the surface of MCM-41 materials providing a very high surface area spherical MCM-41 material was achieved. Electron dispersive spectroscopy (EDS) was performed to display the elemental composition of MCM-41 and 35COF-MCM-41 as displayed in Fig. 3f, g. Figure 3f displays that only two metals existed in the sample which is Si and O which approved that there are no impurities in MCM-41 samples. While, Fig. 3g spectrum of 35COF-MCM-41 displayed the existence of Co, Fe, O, and Si elements with relative percentage of 7.57, 14.83, 41.85 and 35.75%, respectively. As well as, there are no other peaks were appeared in the spectrum, which approved that 35COF-MCM-41 was successfully prepared without any impurities. Additionally, the findings of elemental composition from EDS analysis were confirmed using EDS elemental mapping image as displayed in Fig. 3h, that evidently displayed a homogeneous distribution of cobalt and iron elements in the structure of 35COF-MCM-41 sample.

3.1.3 TEM and Particle Size Distribution Analysis

The morphology and the crystallite size of all the prepared samples were presented in Fig. 4. Figure 4a displays the TEM image mesoporous MCM-41, which reveals that it has a honeycomb-like shape structure with the cylindrical

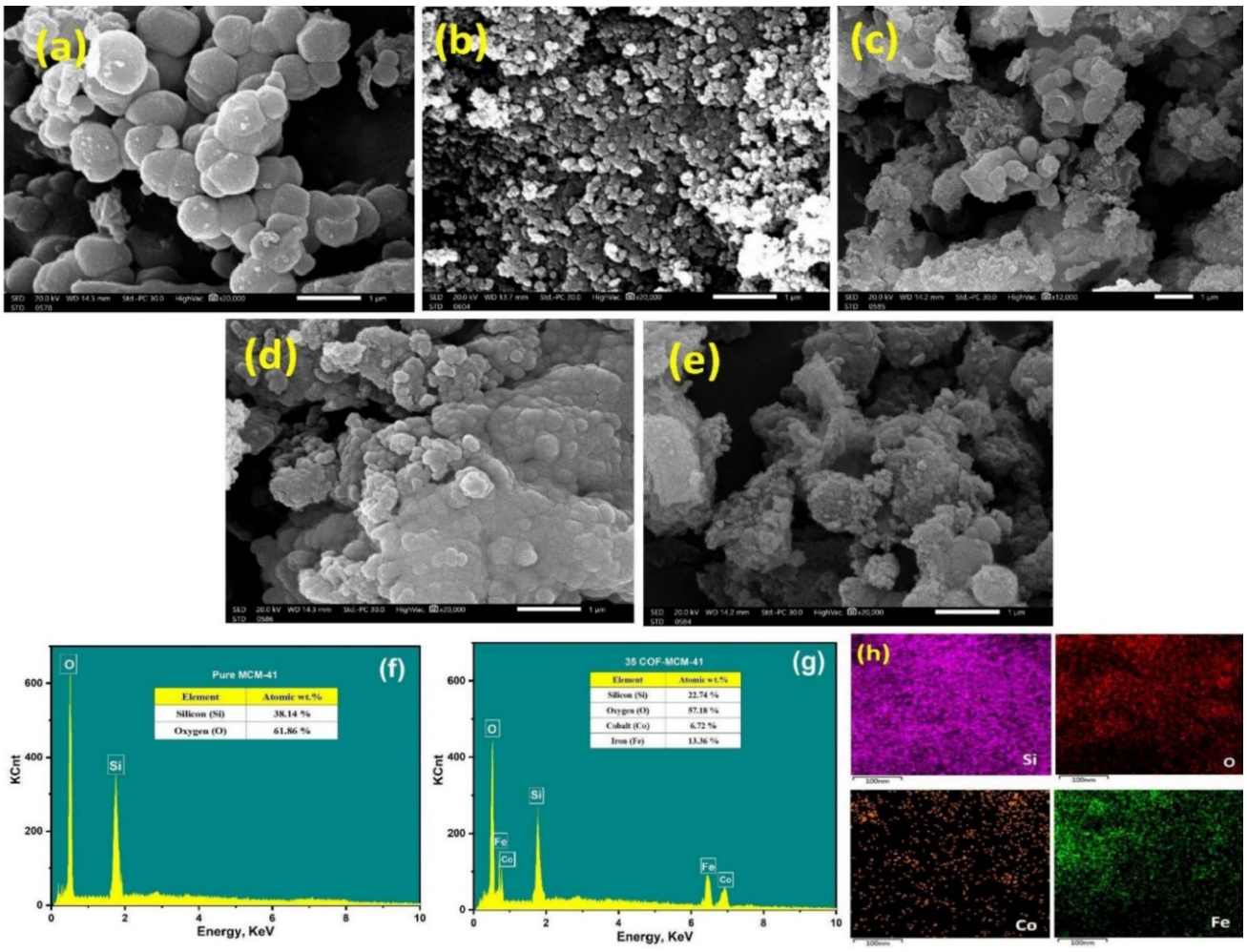

Fig. 3 **a**–**e**SEM images of MCM-41, COF, 15COF-MCM-41, 35COF-MCM-41, and 55COF-MCM-41; **f**, **g** EDS analysis of MCM-41 and 35COF-MCM-41; **h** EDS elemental mapping images of 35COF-MCM-41

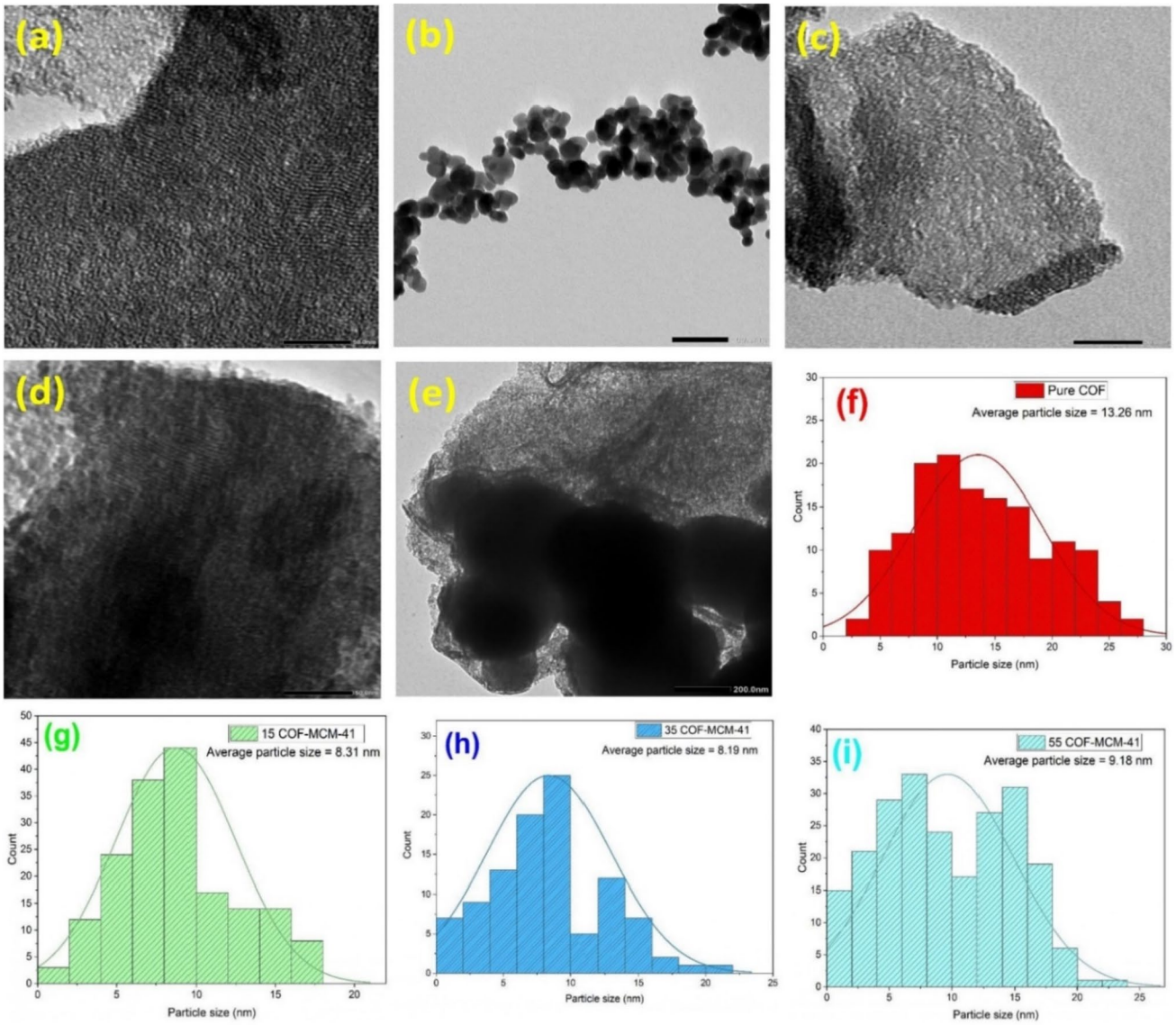

Fig. 4 **a–e** TEM images of MCM-41, COF, 15COF-MCM-41, 35COF-MCM-41, and 55COF-MCM-41; **f–i** nanoparticles size histograms of COF, 15COF-MCM-41, 35COF-MCM-41, and 55COF-MCM-41

hexagonal pores. On the other hand, TEM image of pure COF was displayed in Fig. 4b, which reveals that $CoFe_2O_4$ has a sphere like structure [45, 46]. TEM images of x COF-MCM-41 nano-composites have been displayed in Fig. 4c–e that displayed COF NPs were successfully well dispersed on MCM-41 as a dark spot spherical NPs and its count increased with increase the contents of ferrites until reached a maximum at 55COF-MCM-41. Additionally, the nanoparticle size histogram of COF, 15COF-MCM-41, 35COF-MCM-41, and 55COF-MCM-41 were studied by image J software and displayed in Fig. 4f–i. From these figures, the average particle sizes of COF, 15COF-MCM-41, 35COF-MCM-41, and 55COF-MCM-41NPs were found to be 13.26, 8.31, 8.19, and 9.18 nm, respectively. These results were well fitted with the findings gained from XRD results.

3.1.4 Nitrogen Sorption Measurements

The porosity and textural properties of MCM-41, COF, 15COF-MCM-41, 35COF-MCM-41, and 55COF-MCM-41 were studied through nitrogen sorption isotherms and Brunauer–Emmett–Teller (BET) plots and displayed in Figs. 5 and 6. According to the classification provided by the International Union of Pure and Applied Chemistry (IUPAC), both pure and modified MCM-41 samples exhibit a type IV isotherm. This is characterized by a distinct capillary condensation step, which is considered a unique

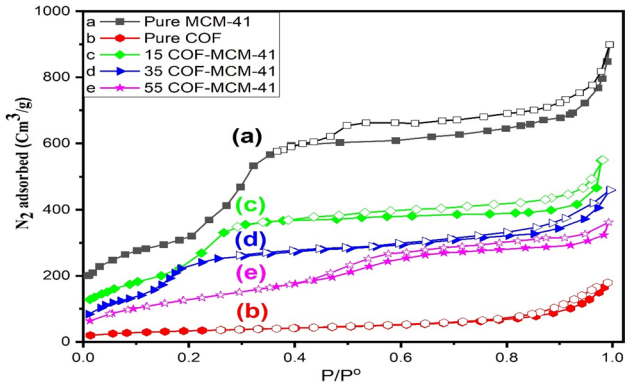

Fig. 5 Nitrogen sorption isotherms of **a** MCM-41, **b** COF, **c** 15COF-MCM-41, **d** 35COF-MCM-41, and **e** 55COF-MCM-41

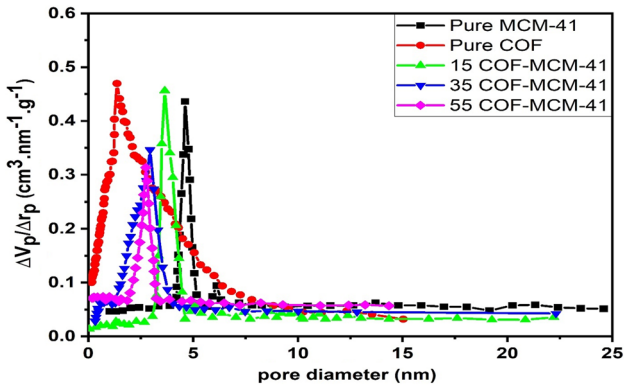

Fig. 6 pore size distribution curves of **a** MCM-41, **b** COF, **c** 15COF-MCM-41, **d** 35COF-MCM-41, and **e** 55COF-MCM-41

characteristic of mesoporous materials, as shown in Fig. 5. As well as, there are three well distinguished regions were observed in all curves that approved the successful preparation of MCM-41: (i) monolayer–multilayer adsorption, (ii) capillary condensation, and (iii) multilayer adsorption on the outer particle surfaces. Nitrogen sorption isotherms of pure and modified MCM-41 show clear hysteresis loop with type H1 at P/P^o ranged from 0.24 and 0.41, which is an evident for the existence of highly ordered mesoporous channels even after deposition of ferrites on MCM-41 surfaces as previously proved in TEM images. As well as, the surface area (S_{BET}) for all the prepared samples was calculated at a P/P^o ranged from 0.01 to 0.35 using nitrogen adsorption data. The results displayed that S_{BET} of MCM-41, COF, 15COF-MCM-41, 35COF-MCM-41, and 55COF-MCM-41 were equal 1441, 117, 1127, 924, and 586 $m^2.\ g^{-1}$, respectively as displayed in Table 1. These decrease in the surface area could be attributed to the deposition of cobalt ferrites nanoparticles on the surface and inside the pores of MCM-41 that can cause blockage and decrease the surface area [47]. The prepared samples exhibit narrow pore size

Table 1 Porosity and texture properties of pure and modified MCM-41

Sample Name	S_{BET} ($m^2.\ g^{-1}$)	V_p ($cm^3.\ g^{-1}$)	D_p (nm)	Crystal size (nm)	
				XRD	TEM
MCM-41	1441	0.978	4.62	–	–
$CoFe_2O_4$	117	0.345	1.51	12.47	13.26
15COF-MCM-41	1127	0.871	3.67	7.87	8.31
35COF-MCM-41	924	0.741	2.94	8.74	8.19
55COF-MCM-41	586	0.585	2.71	9.57	9.18

distribution, which calculated from the desorption branch of the corresponding isotherm and displayed in Fig. 6. According to the data obtained in Table 1, it can be concluded that MCM-41 has the highest S_{BET}, pore size and the total pore volume, and decrease with increasing the contents of cobalt ferrites that could be due to accumulation of $CoFe_2O_4$ on the pores of MCM-41 [48].

3.1.5 Electrochemical Performance

The excellent capacitive properties of the as-synthesized electrodes were evaluated using a three-electrode system. To determine the optimal electrolyte for the electrode that was prepared, a selection process was carried out by performing cyclic voltammetry (CV) measurements with various electrolyte solutions. The electrochemical performances of 35COF-MCM-41 composite were investigated using different electrolyte solutions (H_2SO_4, KOH, and Na_2SO_4) at a concentration of 1.0 M, and the results were displayed in Fig. 7a at a scan rate of 30 mV/sec. H_2SO_4 solution has a greater electrochemical active region, and thus, H_2SO_4 was considered the most suitable electrolyte, which has the highest intensity compared with other electrolytes. Furthermore, the galvanostatic charging and discharging (GCD) behavior of the 35COF-MCM-41 nanocomposite was analyzed using the same electrolytes and the results were shown in Fig. 7b. The curves displayed that the prepared electrode has a quasi-triangular shape, indicating the reduction – oxidation behavior of spinal ferrites on MCM-41. The specific capacitances of 35COF-MCM-41 in different electrolyte were calculated using Eq. (2) and was equaled 345, 574, and 768 F. g^{-1} at 1.0 A. g^{-1} in Na_2SO_4, KOH, and H_2SO_4 solutions, respectively. According to these results, H_2SO_4 is the most suitable electrolyte as confirmed by CV and GCD measurements.

The cyclic voltammograms of MCM-41, COF, 15COF-MCM-41, 35COF-MCM-41, and 55COF-MCM-41 were performed at different scan rates ranged from 5 to 100 mV sec^{-1}. The findings reveal that the specific capacitance is

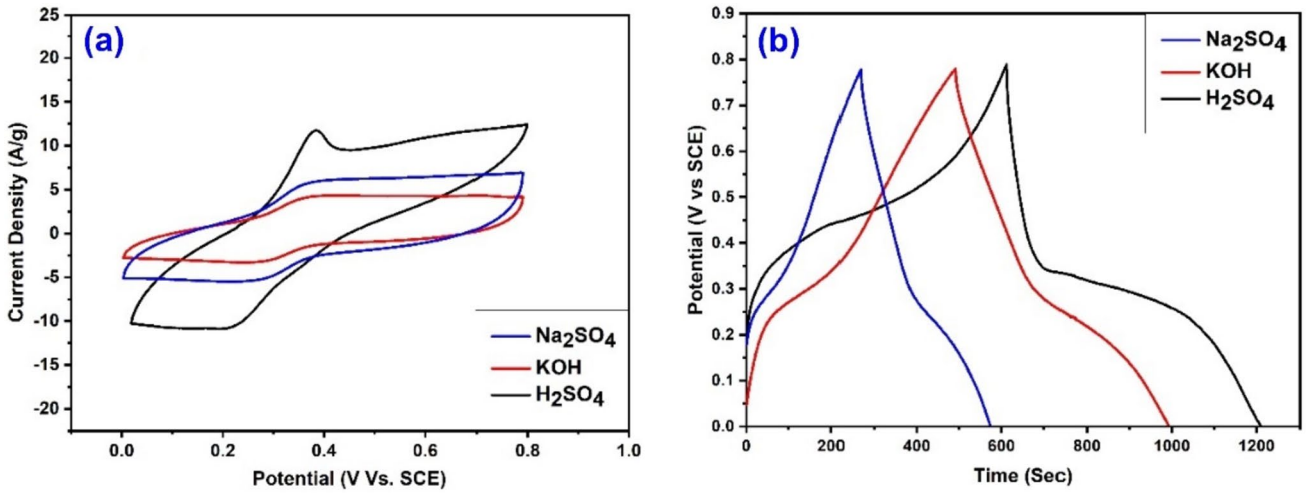

Fig. 7 **a** Cyclic voltammograms (CV) and **b** GCD curves of 35COF-MCM-41 in different electrolyte solution

inversely proportional to the scan rates attributed to electrolyte ions that take adequate time to intercalate the electrode surface. The first electrode is MCM.41, which shows peaks demonstrating redox reactions at a potential window ranging from 0.0 to 0.8V, as shown in Fig. 8a. While, the CV of the COF electrode (Fig. 8b) shows that the enhancement of pseudocapacitance at the same potential window range lead to higher peak intensity than MCM.41. Additionally, after adding spinal ferrites on mesoporous silica, the CV measurements of 15COF-MCM-41, 35COF-MCM-41, and 55COF-MCM-41 electrodes show enhanced pseudocapacitance due to maxima of oxidation and reduction peaks at various scan rates of 100, 50, 30, 20, 10, and 5 mV/sec, as shown in their curves in Fig. 8c–e. All the prepared electrodes show faradic-type capacitive characteristics resulting from the oxidation or reduction of active materials at the electrode. The CV curves show two peaks:

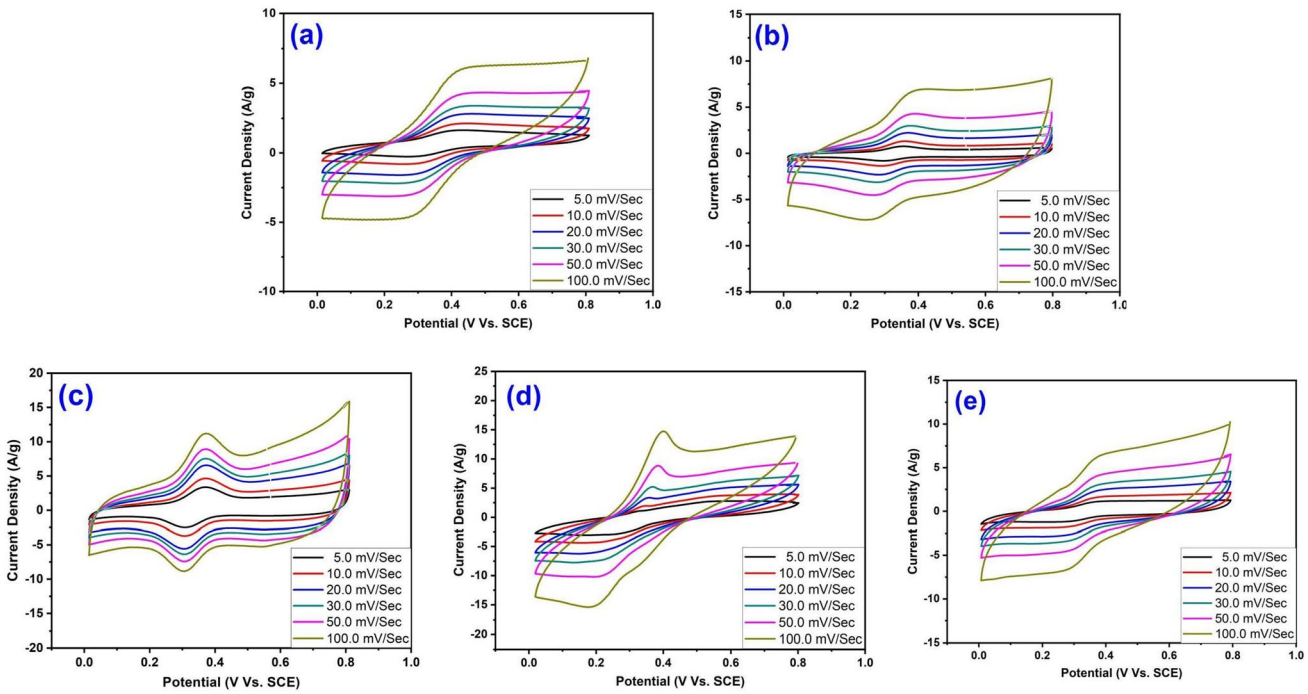

Fig. 8 CV voltammograms at different scan rates of **a** Pure MCM-41, **b** pure COF, **c** 15 COF-MCM-41, **d** 35 COF-MCM-41, and **e** 55 COF-MCM-41

the oxidation peak in positive currents and the reduction peak in negative currents.

The galvanic charge and discharge curves were investigated at different current densities of 1.0, 1.5, 2.0, 2.5, 3.0, 4.0 A. g^{-1} for all the prepared electrodes at potential windows of 0.0 to 0.8V, and displayed in Fig. 9. Based on the information presented in the figures, it can be observed that when the electrode material operates at a higher current density, the discharge time is shorter. This is because there is insufficient time for the aqueous electrolyte ions to diffuse into the inner pores of the electrode and establish proper contact, resulting in reduced capacitive [49–52]. MCM.41 electrode in Fig. 9a shows pseudocapacitive performance, which approves the redox reaction throughout the charge discharge processes and affirms the outcomes obtained from CV curves. While, GCD of COF nanocomposite (Fig. 9b) verifies the outcomes of CV curves that obtain enhanced capacitive performance in comparison to MCM.41 that show specific capacitance higher than MCM-41 as displayed in Table 2. When cobalt ferrites and MCM-41 were mixed together, the specific capacitances of 15COF-MCM-41, 35COF-MCM-41, and 55COF-MCM-41 electrodes were doubled which may be due to the synergetic effect between the spinal ferrites and MCM-41. The capacitive performance at different current densities were calculated from Eq. (2) and its values were displayed in Table 2. In addition, each GCD curve exhibits a discharge platform due to Faraday redox reactions, which confirms the pseudocapacitance property of the electrode material. This property is also confirmed by the presence of redox peaks in the CV curves. Furthermore, the GCD curves of pure and modified MCM-41 were conducted at a current density of 1.0 A. g^{-1} and presented in Fig. 9f. The figure shows that all the samples exhibit a quasi-triangular shaped GCD curve,

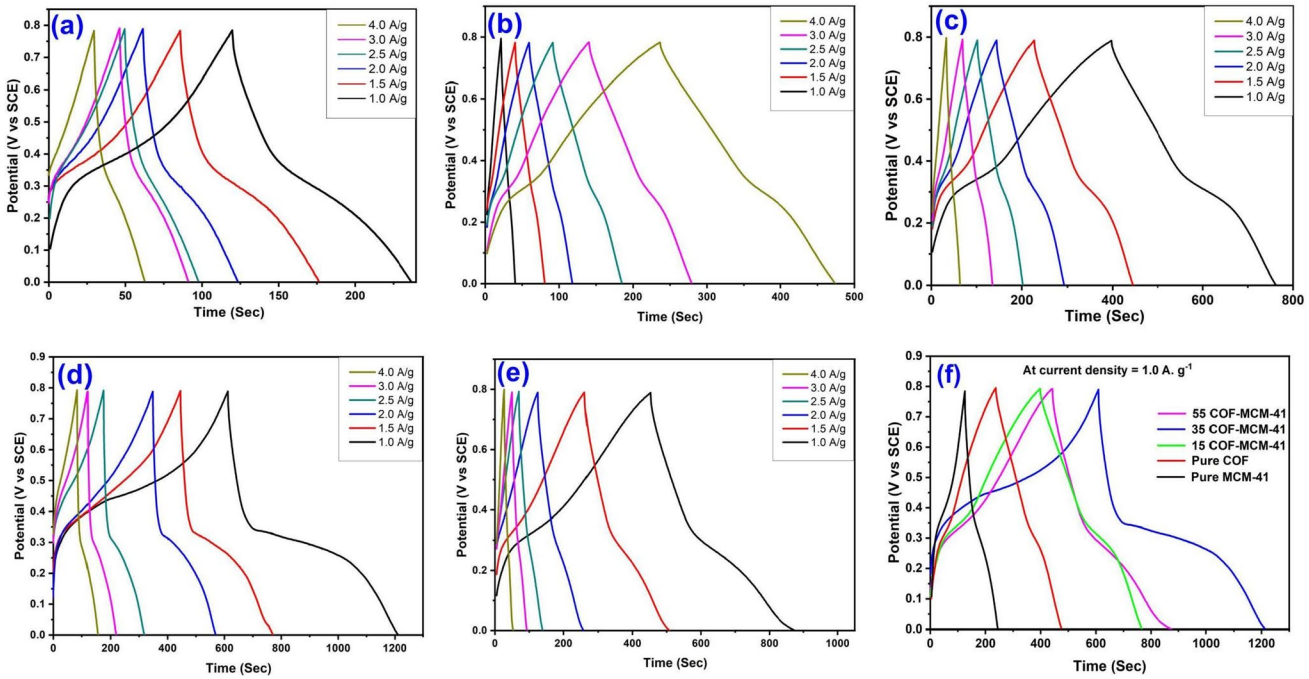

Fig. 9 GCD curves at different current density of **a** Pure MCM-41, **b** pure COF, **c** 15 COF-MCM-41, **d** 35 COF-MCM-41, **e** 55 COF-MCM-41 and **f** GCD curves for all the prepared electrodes at current density of 1.0 A- g^{-1}

Table 2 specific capacitances of the prepared electrodes at different current densities using GCD curves and its EIS measurements

Sample name	Specific capacitance (F. g^{-1}) at different current densities						EIS Measurement	
	1.0 A. g^{-1}	1.5 A. g^{-1}	2.0 A. g^{-1}	2.5 A. g^{-1}	3.0 A. g^{-1}	4.0 A. g^{-1}	R_s Ω	R_{ct} Ω
Pure MCM.41	156	151	145	137	127	115	22.5	21.8
Pure COF	286	245	223	181	154	100	20.2	19.5
15 COF-MCM-41	458	407	372	319	251	160	17.7	17.1
35 COF-MCM-41	746	616	557	462	382	370	12.3	11.2
55 COF-MCM-41	532	467	332	222	154	135	15.2	14.9

representing the redox behavior of the prepared electrodes. Higher loading (35 and 55%) could influence the kinetics of ion diffusion within the electrode material. A discharge plateau might indicate that at higher current densities, the kinetics of ion diffusion become more significant, leading to a plateau-like shape rather than a quasi-triangular one. As well as, the different loading percentages may affect the filling of mesopores within the MCM-41 structure. Higher loading could result in more complete pore filling, influencing ion accessibility and contributing to a plateau-like discharge shape [53]. The specific capacitances were found to be 156, 286, 458, 746, and 532 $F.g^{-1}$ for MCM-41, COF, 15COF-MCM-41, 35COF-MCM-41, and 55COF-MCM-41, respectively at a current density of 1.0 A. g^{-1}. The specific capacitance was raised with increasing the ferrites content until reached a maximum value at 35COF-MCM-41. Afterward, it decreased again. The main reason for this high specific surface area could be related to the good dispersion of cobalt ferrites on the surface of MCM-41 and the small particle size as confirmed by TEM and XRD patterns. While, the reduction if specific capacitance after 35 wt.% of ferrites may be related to the aggregation of COF nanoparticles on MCM-41 surface, which blocking the mesoporous structure of MCM-41 and hindering the diffusion of electrolyte ions within the electrode.

To assess the electrode's performance in real-world applications, the electrochemical properties of an asymmetric supercapacitor (ASC) using 35COF-MCM-41 were tested. ASC typically consist of two electrodes with different properties, such as one electrode activated carbon and the other electrode with high pseudocapacitance. In this study, the 35COF-MCM-41 electrode was used as the pseudocapacitive electrode, and its electrochemical performance was evaluated in an ASC configuration. The cyclic voltammetry (CV) analysis of the electrode was conducted at different scan rates (Fig. 10a) and a potential window of 0.0 to 1.0 mV, which showed significant Faradaic redox reaction effects on capacitance and pseudocapacitive properties due to its almost distorted rectangular shape. The cobalt ferrites exhibit favorable electrochemical behavior due to the

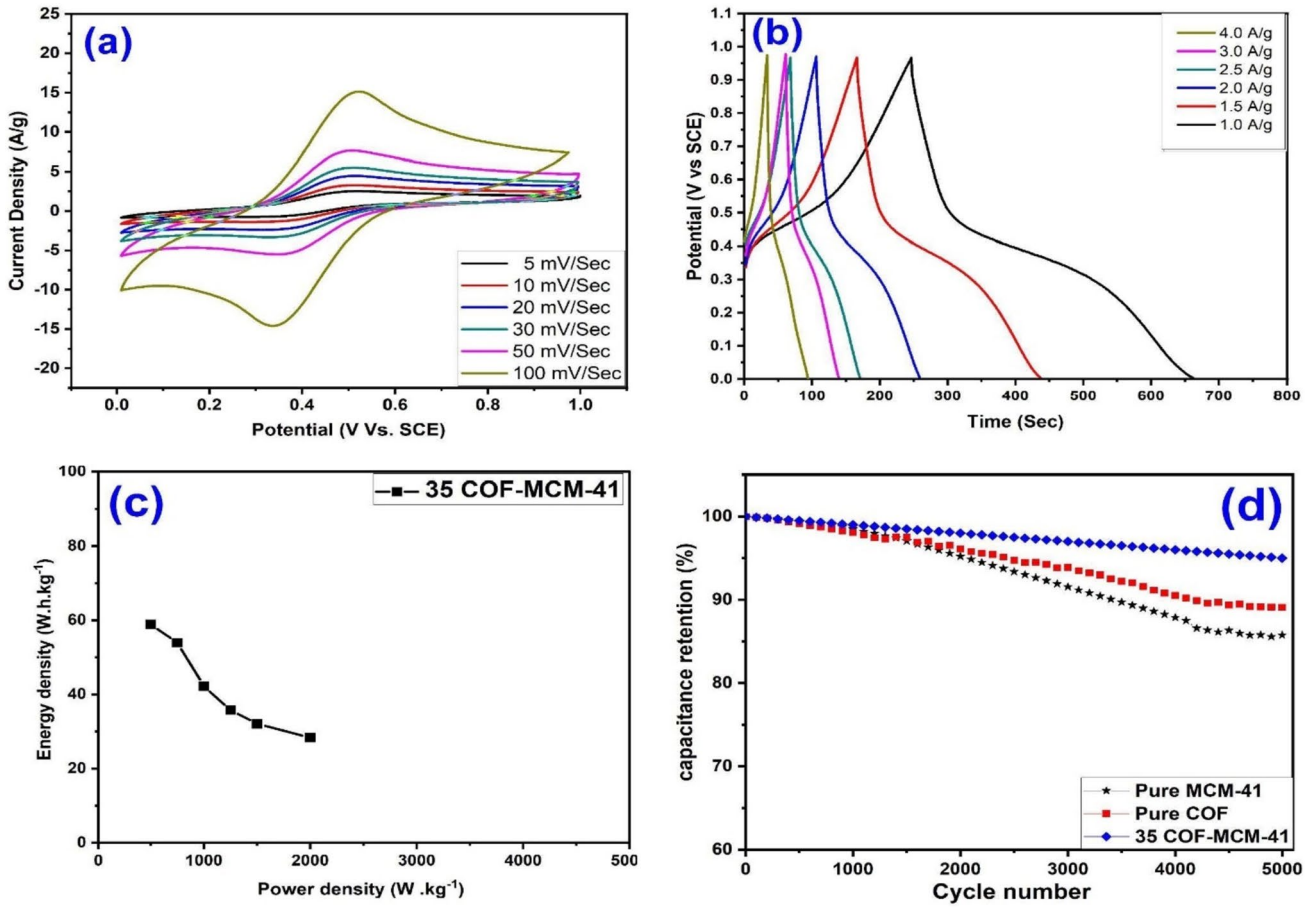

Fig. 10 **a** Cyclic voltammograms of asymmetric 35COF-MCM-41 electrode at different scan rates and **b** GCD curves of asymmetric 35COF-MCM-41 electrode at different current density, **c** Ragone plot of asymmetric 35COF-MCM-41 electrode, and **d** cyclic stability of MCM-41, COF, and 35COF-MCM-41 electrodes

presence of cobalt and iron ions. These ions play a crucial role in the redox reactions that occur during the charging and discharging processes of the supercapacitor. During the charging process, the cobalt ions (Co^{2+}) are oxidized to cobalt oxyhydroxides (CoOOH) or cobalt hydroxides ($Co(OH)_2$), while the iron ions (Fe^{3+}) are reduced to iron oxyhydroxides (FeOOH) or iron hydroxides ($Fe(OH)_3$). This oxidation–reduction reaction allows for the storage of electrical energy within the supercapacitor. On the other hand, during the discharging process, the cobalt oxyhydroxides or cobalt hydroxides are reduced back to cobalt ions, while the iron hydroxides are oxidized back to iron ions. This reversal of the redox reactions releases the stored electrical energy, which can be utilized for various applications [54].

Furthermore, the galvanostatic charge–discharge (GCD) curves were measured at different current densities (Fig. 10b), which allowed the calculation of the asymmetric specific capacitances of 35COF-MCM-41. The specific capacitance of 35COF-MCM-41 at current density of 1.0, 1.5, 2.0, 2.5, 3.0 and 4.0 A. g^{-1} was found to be 204, 231, 257, 304, 388, and 424 F. g^{-1}, respectively. Also, the energy and power densities of 35COF-MCM-41 were determined from Eqs. (3) and (4), and a Ragone plot was constructed to compare its performance with other reported asymmetric devices as displayed in Fig. 10c. The energy and power density of 35COF-MCM-41 were evaluated at various current densities, and the highest values were obtained at a current density of 1.0 A·g^{-1}. The maximum energy density reached 58.89 W·h·kg-1, while the power density reached 500 W·kg^{-1}. These energy density results were comparable to, or even superior to, those reported for asymmetric devices in previous studies [55–57]. The cycle stability of the electrodes was evaluated by measuring the capacitance retention of MCM-41, COF, and 35COF-MCM-41 electrodes over 5000 cycles at a current density of 3.0 A. g^{-1} and displayed in Fig. 10d. The findings demonstrated that among the tested electrodes, 35COF-MCM-41 exhibited the most superior electrochemical performance and cycle stability. After 5000 cycles, it retained 94.8% of its capacitance. In comparison, MCM-41 and COF showed capacitance retentions of 84.4% and 89.4%, respectively.

Electrochemical impedance spectroscopy (EIS) was conducted on the prepared electrodes within a frequency range of 100 mHz to 100 kHz while maintaining an open circuit potential. The EIS results, displayed in Fig. 11, exhibit a depressed semi-circle in the middle frequencies, indicating the porosity of the electrode. At low frequencies, a steep linear curve suggests the diffusion of ions. The charge transfer resistance (R_{ct}), obtained from the semicircle diameter, represents the interface resistance between the electrolyte and electrode. The capacitive component of the prepared electrodes is also considered in this calculation [58, 59]. The ohmic series resistance (R_s), determined from the intercept

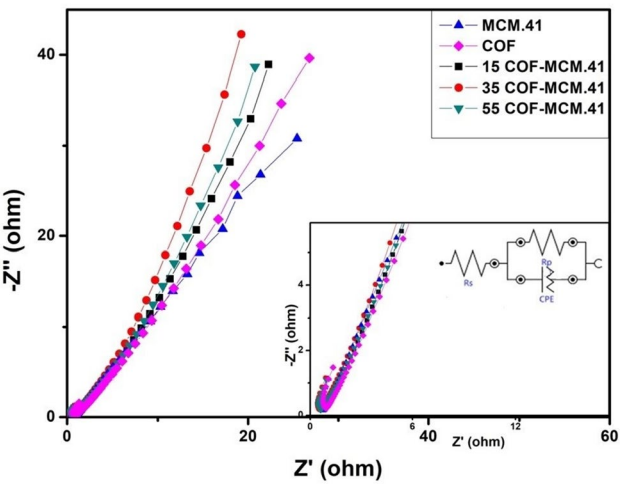

Fig. 11 Nyquist plots as a function of frequency of MCM-41, COF, 15COF-MCM-41, 35COF-MCM-41, and 55COF-MCM-41 electrodes, Inset displays the results in high-frequency region

of the (Z'-axis), reflects the combined intrinsic resistance of the active materials, ionic resistance of the electrolyte, and contact resistance with the current collector. Using NOVA 2.1.4 software, the R_{ct} and R_s values were calculated and are presented in Table 2. The results demonstrate that the 35COF-MCM-41 electrode exhibits the lowest charge transfer resistance (R_{ct}) and ohmic series resistance (R_s) among the other electrodes. This is attributed to the superior homogeneous distribution of nanoparticles within the 35COF-MCM-41 electrode, affirming its excellent electrochemical performance.

4 Conclusion

In this work, MCM.41 was prepared from cetyltrimethylammonium bromide (CTAB) as a template and tetraethyl orthosilicate (TEOS), then different weight ratios of cobalt ferrites $CoFe_2O_4$ (15, 35, and 55 wt.%) were loaded to MCM.41. The XRD analysis showed that the nanoparticles were ranged from 8 – 14 nm, which align with the TEM Images. As well as, SEM and TEM images reveals that the number of nanoparticles deposited on the surface of MCM.41 were increased with increasing the contents of ferrites until aggregation occurred at the maximum weight ratios, which decrease the electrochemical performance. These results fit in with the electrochemical performance, which reveals that the specific capacitance went through a dramatic increase until the weight ratio of the 35COF-MCM-41 electrode equaled 746.0 F. g^{-1}. Moreover, the 35COF-MCM-41 electrode showed superior cyclic performance after 5000 cycles with cyclic retention equal to 94.8% in comparison to the MCM-41 electrode and the COF electrode, which showed

capacitance retention of 84.4 and 89.4%, respectively. Furthermore, asymmetric supercapacitor (ASC) using 35COF-MCM-41 displayed that the energy and power density of 35COF-MCM-41 was calculated at different current density and reached a maximum values of energy density 58.89 W.h.kg^{-1} and power density 500 W kg^{-1} at current density of 1.0 A. g^{-1}.

Author Contributions AN, RHA, RAS; validation, resources, visualization, supervision, and Funding acquisition: MSG; Conceptualization, methodology, formal analysis, investigation, and visualization; FSA; Conceptualization, methodology, formal analysis, investigation, visualization, and supervision, RSS; Conceptualization, validation, writing—review and editing and Funding acquisition. All authors have read and agreed to the published version of the manuscript.

Acknowledgement The authors extend their sincere appreciation to Researchers Supporting Project number (RSP2024R442), King Saud University, Riyadh, Saudi Arabia, for partial funding of this work.

Data Availability Available upon request.

Declarations

Conflict of interest The author(s) declared no potential conflicts of interest with respect to the research, authorship, and/or publication of this article.

References

1. J. Ji, S. Park, J.H. Choi, Morphology engineering of hybrid supercapacitor electrodes from hierarchical stem-like carbon networks with flower-like MoS2 structures. ACS Omega (2023). https://doi.org/10.1021/acsomega.3c00445
2. A. Barjola, A. Rapeyko, O. Sahuquillo, F..X.. Llabrés, I. Xamena, E.. Giménez, AgBTC MOF-mediated approach to synthesize silver nanoparticles decorated on reduced graphene oxide (rGO@Ag) for energy storage applications. ACS Appl. Energy Mater. (2023). https://doi.org/10.1021/acsaem.2c03872
3. M.S. Gouda, M. Shehab, S. Helmy, M. Soliman, R.S. Salama, Nickel and cobalt oxides supported on activated carbon derived from willow catkin for efficient supercapacitor electrode. J. Energy Storage. **61**, 106806 (2023)
4. A.H. Anwer, M.Z. Ansari, F. Mashkoor, S. Zhu, M. Shoeb, C. Jeong, Synergistic effect of carbon nanotube and tri-metallic MOF nanoarchitecture for electrochemical high-performance asymmetric supercapacitor applications and their charge storage mechanism. J. Alloys Compd. **955**, 170038 (2023)
5. B.M. Al-Maswari, N. Al-Zaqri, K. Alkanad, F.H. AlOstoot, A. Boshaala, R.T. Radhika, B.M. Venkatesha, Magnesium bismuth ferrite nitrogen-doped carbon nanomagnetic perovskite: synthesis and characterization as a high-performance electrode in a supercapacitor for energy storage. ACS Omega (2023). https://doi.org/10.1021/acsomega.3c00259
6. M. Khot, R.S. Shaik, W. Touseef, A. Kiani, Binder-free NiO/CuO hybrid structure via ULPING (Ultra-short Laser Pulse for In-situ Nanostructure Generation) technique for supercapacitor electrode. Sci. Rep. **13**, 6975 (2023)
7. M.M.M. Mostafa, A.A. Alshehri, R.S. Salama, High performance of supercapacitor based on alumina nanoparticles derived from Coca-Cola cans. J. Energy Storage. **64**, 107168 (2023)
8. E. Payami, M.A. Keynezhad, K.D. Safa, R. Teimuri-Mofrad, Development of high-performance supercapacitor based on Fe3O4@ SiO2@ PolyFc nanoparticles via surface-initiated radical polymerization. Electrochim. Acta **439**, 141663 (2023)
9. P. Yadav, M.K. Raju, R.K. Samudrala, M. Gangadhar, J. Pani, H. Borkar, P.A. Azeem, Cost-effective akermanite derived from industrial waste for working electrodes in supercapacitor applications. New J. Chem. **47**, 3255–3265 (2023)
10. S. Huang, D. Bi, Y. Xia, H. Lin, Facile construction of three-dimensional architectures of a nanostructured polypyrrole on carbon nanotube fibers and their effect on supercapacitor performance. ACS Appl. Energy Mater. (2023). https://doi.org/10.1021/acsaem.2c03167
11. A. Chonat, Mini-review on conducting polymer–MoS2–carbon ternary composite as a hybrid electrode material for supercapacitor applications: progress and perspectives. Energy Fuels **37**, 3555–3569 (2023)
12. A.G. Olabi, Q. Abbas, A. Al Makky, M.A. Abdelkareem, Supercapacitors as next generation energy storage devices: properties and applications. Energy **248**, 123617 (2022)
13. R. Salama, S. Abd Elhakim, S. Samra, S. El-Dafrawy, A.A. Ibrahim, A. Ahmed, Synthesis, characterization of titania supported on mesoporous MCM-41 and its application for the removal of methylene blue. Delta Univ. Sci. J. **5**, 321–339 (2022)
14. R.S. Jassas, A.A. Alsimaree, S.A. Ahmed, R.S. Salama, Enhanced catalytic activity for CO oxidation by highly active pd nanoparticles supported on reduced graphene oxide / copper metal organic framework. J. Taiwan Inst. Chem. Eng. **000**, 1–15 (2021). https://doi.org/10.1016/j.jtice.2021.08.034
15. F. BoorboorAjdari, M.I. Ostad, M.N. Shahrak, M. Ershadi, S.S. Malek, F. Ghasemi, Y. Zolfaghari, S. Ramakrishna, Investigating MCM-41/metal-organic framework nanocomposites as silicon-containing electrodes for supercapacitor. Surfaces and Interfaces. **29**, 101796 (2022)
16. S. Divyadharshini, R. Pachaiappan, J.M. Fernandes, R. Rathika, D.P. Joseph, M. Kovendhan, Potential impact of smart-hybrid supercapacitors in novel electronic devices and electric vehicles. Smart Supercapacitors (2023). https://doi.org/10.1016/B978-0-323-90530-5.00026-5
17. K. Zhu, C. Jin, Z. Klencsár, J. Wang, Fabrication of yolk/shell partially inverse spinel cobalt ferrite/mesoporous silica nanostructured catalysts for organic pollutants degradation by peroxymonosulfate activation. Catal. Letters. **147**, 1732–1743 (2017)
18. M. Gharibshahian, O. Mirzaee, M.S. Nourbakhsh, Evaluation of superparamagnetic and biocompatible properties of mesoporous silica coated cobalt ferrite nanoparticles synthesized via microwave modified Pechini method. J. Magn. Magn. Mater. **425**, 48–56 (2017)
19. T.S. Saleh, A.K. Badawi, R.S. Salama, M.M.M. Mostafa, Design and development of novel composites containing nickel ferrites supported on activated carbon derived from agricultural wastes and its application in water remediation. Materials (Basel). **16**, 2170 (2023)
20. F.T. Alshorifi, A.A. Alswat, R.S. Salama, Gold-selenide quantum dots supported onto cesium ferrite nanocomposites for the efficient degradation of rhodamine B. Heliyon. **8**, e09652 (2022)
21. D.E. Tobbala, A.S. Rashed, R.S. Salama, T.I. Ahmed, Performance enhancement of reinforced concrete exposed to electrochemical magnesium chloride using nano-ferrite zinc-rich epoxy. J. Build. Eng. **57**, 104869 (2022)
22. S.A. El-Hakam, A.A. Ibrahim, L.A. Elatwy, W.S.A. El-Yazeed, R.S. Salama, Y.G.A. El-Reash, A.I. Ahmed, Greener route for the removal of toxic heavy metals and synthesis of 14-aryl-14H dibenzo[a, j] xanthene using a novel and efficient Ag-Mg bimetallic MOF as a recyclable heterogeneous nanocatalyst. J. Taiwan

Inst. Chem. Eng. **122**, 176–189 (2021). https://doi.org/10.1016/j.jtice.2021.04.036
23. A. Soufi, H. Hajjaoui, R. Elmoubarki, M. Abdennouri, S. Qourzal, N. Barka, Spinel ferrites nanoparticles: Synthesis methods and application in heterogeneous Fenton oxidation of organic pollutants–A review. Appl. Surf. Sci. Adv. **6**, 100145 (2021)
24. A.N. Alqarni, E. Cevik, M.A. Gondal, M.A. Almessiere, A. Baykal, A. Bozkurt, Y. Slimani, M. Hassan, A. Iqbal, S.A. Alotaibi, Synthesis and design of vanadium intercalated spinal ferrite (Co0.5Ni0.5VxFe1.6−xO4) electrodes for high current supercapacitor applications. J. Energy Storage **51**, 104357 (2022)
25. M. Minakshi, D.R.G. Mitchell, A.R. Munnangi, A.J. Barlow, M. Fichtner, New insights into the electrochemistry of magnesium molybdate hierarchical architectures for high performance sodium devices. Nanoscale **10**, 13277–13288 (2018)
26. M. Minakshi, D.R.G. Mitchell, C. Baur, J. Chable, A.J. Barlow, M. Fichtner, A. Banerjee, S. Chakraborty, R. Ahuja, Phase evolution in calcium molybdate nanoparticles as a function of synthesis temperature and its electrochemical effect on energy storage. Nanoscale Adv. **1**, 565–580 (2019)
27. P. Sharma, M. Minakshi Sundaram, T. Watcharatharapong, S. Jungthawan, R. Ahuja, Tuning the nanoparticle interfacial properties and stability of the core–shell structure in Zn-doped NiMoO4@AWO4. ACS Appl. Mater. Interfaces **13**, 56116–56130 (2021)
28. J.S. Beck, J.C. Vartuli, W.J. Roth, M.E. Leonowicz, C.T. Kresge, K.D. Schmitt, C.T.W. Chu, D.H. Olson, E.W. Sheppard, S.B. McCullen, A new family of mesoporous molecular sieves prepared with liquid crystal templates. J. Am. Chem. Soc. **114**, 10834–10843 (1992)
29. S.A. El-Hakam, S.E. Samra, S.M. El-Dafrawy, A.A. Ibrahim, R.S. Salama, Surface acidity and catalytic activity of sulfated titania supported on mesoporous MCM-41. Int. J. Mod. Chem. **5**, 55–70 (2013)
30. S. Karmakar, B. Panda, B. Sahoo, K.L. Routray, S. Varma, D. Behera, A study on optical and dielectric properties of Ni-ZnO nanocomposite. Mater. Sci. Semicond. Process. **88**, 198–206 (2018)
31. S. Karmakar, K.L. Routray, B. Panda, B. Sahoo, D. Behera, Construction of core@ shell nanostructured NiFe2O4@ TiO2 ferrite NAND logic gate using fluorescence quenching mechanism for TiO2 sensing. J. Alloys Compd. **765**, 527–537 (2018)
32. S. Karmakar, D. Behera, High-temperature impedance and alternating current conduction mechanism of Ni 0.5 Zn 0.5 WO 4 micro-crystal for electrical energy storage application. J. Aust. Ceram. Soc. **56**, 1253–1259 (2020)
33. M.C. Fite, P.-J. Wang, T. Imae, Symmetric and asymmetric supercapacitors of ITO glass and film electrodes consisting of carbon dot and magnetite. Batteries **9**, 162 (2023)
34. M. Khairy, W.A. Bayoumy, K.F. Qasim, E. El-Shereafy, M.A. Mousa, Ternary V-doped Li4Ti5O12-polyaniline-graphene nanostructure with enhanced electrochemical capacitance performance. Mater. Sci. Eng. B **271**, 115312 (2021)
35. K.F. Qasim, M.A. Mousa, Effect of oxidizer on PANI for producing BaTiO3@ PANI perovskite composites and their electrical and electrochemical properties. J. Inorg. Organomet. Polym. Mater. **32**, 1–13 (2022)
36. A.A. Ibrahim, R.S. Salama, S.A. El-Hakam, A.S. Khder, A.I. Ahmed, Synthesis of 12-Tungestophosphoric Acid Supported on Zr/MCM-41 Composite with Excellent Heterogeneous Catalyst and Promising Adsorbent of Methylene Blue. Colloids Surfaces A Physicochem. Eng. Asp. **631**, 127753 (2021)
37. R.S. Salama, S.M. El-Bahy, M.A. Mannaa, Sulfamic acid supported on mesoporous MCM-41 as a novel, efficient and reusable heterogenous solid acid catalyst for synthesis of xanthene, dihydropyrimidinone and coumarin derivatives. Colloids Surfaces A Physicochem. Eng. Asp. **628**, 127261 (2021)
38. M. Popova, Á. Szegedi, K. Lázár, Z. Károly, The physicochemical and catalytic properties of ferrite-containing MCM-41 and SBA-15 materials. Microporous Mesoporous Mater. **151**, 180–187 (2012)
39. H.R. Emamian, A. Honarbakhsh-Raouf, A. Ataie, A. Yourdkhani, Synthesis and magnetic characterization of MCM-41/CoFe2O4 nano-composite. J. Alloys Compd. **480**, 681–683 (2009)
40. A.A. Ibrahim, R.S. Salama, S.A. El-Hakam, A.S. Khder, A.I. Ahmed, Synthesis of sulfated zirconium supported MCM-41 composite with high-rate adsorption of methylene blue and excellent heterogeneous catalyst. Colloids Surfaces A Physicochem. Eng. Asp. **616**, 126361 (2021)
41. W.S.A. El-Yazeed, S.A. El-Hakam, R.S. Salama, A.A. Ibrahim, A.I. Ahmed, Ag-PMA supported on MCM-41: surface acidity and catalytic activity. J. Sol-Gel Sci. Technol. **102**, 387–399 (2022)
42. M.A. Mannaa, H.M. Altass, R.S. Salama, MCM-41 grafted with citric acid: the role of carboxylic groups in enhancing the synthesis of xanthenes and removal of heavy metal ions. Environ. Nanotechnol. Monit. Manag. **15**, 100410 (2020)
43. M.S.A. Salam, M.A. Betiha, S.A. Shaban, A.M. Elsabagh, R.M. Abd El-Aal, Synthesis and characterization of MCM-41-supported nano zirconia catalysts. Egypt. J. Pet. **24**, 49–57 (2015)
44. H. Qin, Y. He, P. Xu, D. Huang, Z. Wang, H. Wang, Z. Wang, Y. Zhao, Q. Tian, C. Wang, Spinel ferrites (MFe2O4): Synthesis, improvement and catalytic application in environment and energy field. Adv. Colloid Interface Sci. **294**, 102486 (2021)
45. R. Samal, B. Dash, C.K. Sarangi, K. Sanjay, T. Subbaiah, G. Senanayake, M. Minakshi, Influence of synthesis temperature on the growth and surface morphology of Co3O4 nanocubes for supercapacitor applications. Nanomaterials **7**, 356 (2017)
46. M.J. Barmi, M. Minakshi, Tuning the redox properties of the nanostructured CoMoO4 electrode: effects of surfactant content and synthesis temperature. ChemPlusChem **81**, 964–977 (2016)
47. P. Kalita, N.M. Gupta, R. Kumar, Solvent-free mukaiyama-aldol condensation catalyzed by Ce–Al–MCM-41 mesoporous materials. Microporous Mesoporous Mater. **144**, 82–90 (2011)
48. R.S. Salama, E.S.M. El-Sayed, S.M. El-Bahy, F.S. Awad, Silver nanoparticles supported on UiO-66 (Zr): As an efficient and recyclable heterogeneous catalyst and efficient adsorbent for removal of indigo carmine. Colloids Surfaces A Physicochem. Eng. Asp. **626**, 127089 (2021). https://doi.org/10.1016/j.colsurfa.2021.127089
49. S. Karmakar, C.D. Mistari, A. Vaidyanathan, M.A. More, B. Chakraborty, D. Behera, Comparison of electrochemical response and electric field emission characteristics of pristine La2NiO4 and La2NiO4/CNT composites: Origin of multi-functionality with theoretical penetration by density functional theory. Electrochim. Acta **369**, 137676 (2021)
50. S. Karmakar, C.D. Mistari, A.S. Shajahan, M.A. More, B. Chakraborty, D. Behera, Enhancement of pseudocapacitive behavior, cyclic performance, and field emission characteristics of reduced graphene oxide reinforced NiGa2O4 nanostructured electrode: a first principles calculation to correlate with experimental observation. J. Phys. Chem. C **125**, 7898–7912 (2021)
51. S. Karmakar, R. Boddhula, B. Sahoo, B. Raviteja, D. Behera, Electrochemical performance of heterogeneous, mesopores and non-centrosymmetric Core@ shell NiCo2O4@ MnO2 nanocomposites and its MWCNT blended complex for supercapacitor applications. J. Solid State Chem. **280**, 121013 (2019)
52. S. Karmakar, S. Taqy, R. Droopad, R.K. Trivedi, B. Chakraborty, A. Haque, Highly stable electrochemical supercapacitor performance of self-assembled ferromagnetic Q-carbon. ACS Appl. Mater. Interfaces **15**, 8305–8318 (2023)
53. J. Liu, J. Wang, C. Xu, H. Jiang, C. Li, L. Zhang, J. Lin, Z.X. Shen, Advanced energy storage devices: basic principles,

analytical methods, and rational materials design. Adv. Sci. **5**, 1700322 (2018)
54. F. Zhou, Q. Liu, J. Gu, W. Zhang, D. Zhang, A facile low-temperature synthesis of highly distributed and size-tunable cobalt oxide nanoparticles anchored on activated carbon for supercapacitors. J. Power. Sources **273**, 945–953 (2015)
55. H. Xuan, G. Lin, F. Wang, J. Liu, X. Dong, F. Xi, Preparation of biomass-activated porous carbons derived from torreya grandis shell for high-performance supercapacitor. J. Solid State Electrochem. **21**, 2241–2249 (2017)
56. Y. Gogotsi, P. Simon, True performance metrics in electrochemical energy storage. Science **334**, 917–918 (2011)
57. Z. Wen, X. Wang, S. Mao, Z. Bo, H. Kim, S. Cui, G. Lu, X. Feng, J. Chen, Crumpled nitrogen-doped graphene nanosheets with ultrahigh pore volume for high-performance supercapacitor. Adv. Mater. **24**, 5610–5616 (2012)
58. H.S. Magar, R.Y.A. Hassan, A. Mulchandani, Electrochemical impedance spectroscopy (EIS): principles, construction, and biosensing applications. Sensors **21**, 6578 (2021)
59. A. Sobhani-Nasab, H. Naderi, M. Rahimi-Nasrabadi, M.R. Ganjali, Evaluation of supercapacitive behavior of samarium tungstate nanoparticles synthesized via sonochemical method. J. Mater. Sci. Mater. Electron. **28**, 8588–8595 (2017)